Climate and Surface Mass Balance at Glaciar Perito Moreno, Southern Patagonia

Masahiro Minowa[ⓘ],[a] Pedro Skvarca,[b] and Koji Fujita[ⓘ][a]

[a] *Graduate School of Environmental Studies, Nagoya University, Nagoya, Japan*
[b] *Glaciarium–Glacier Interpretive Center, El Calafate, Argentina*

ABSTRACT: The mass budget of southern Patagonian glaciers is characterized by an extreme amount of surface ablation. To understand the processes controlling surface mass balance, we analyzed in situ data including meteorological variables and ablation stakes for the 25 years between 1996 and 2020 near the terminus of Glaciar Perito Moreno in southern Patagonia in South America. The mean annual temperature has increased over the study period at a rate of 0.2°C decade^{-1}. An energy-balance model was applied to calculate a point surface mass balance, based on meteorological records. The average point surface mass balance is estimated to be -16.3 m water equivalent (w.e.) yr^{-1} between 1996 and 2020, decreasing at a rate in the range from -0.4 to -0.9 m w.e. yr^{-1} decade^{-1}. The greatest contribution to the surface energy balance was due to the sensible heat flux, and its variation drove the surface mass balance variation. The meteorological and surface mass balance records were compared with the Southern Annular Mode and El Niño–Southern Oscillation, which change the atmospheric circulation over southern Patagonia and influence surface mass balance near the terminus of the glacier. Our long-term dataset investigates the detailed meteorological conditions and surface mass balance and their connection with the large-scale climate variability over the last 25 years, reported for the first time in Patagonia.

KEYWORDS: Glaciers; Climate change; Climate records

1. Introduction

Over the last several decades, the glaciers in southern Patagonia have experienced one of the fastest mass losses in the world (e.g., Zemp et al. 2019). The two major ice masses, the northern and the southern Patagonian ice-fields, have shown the largest mass loss in South America (e.g., Braun et al. 2019; Dussaillant et al. 2019). Both ice-fields are characterized by calving glaciers that flow into fjords or lakes (Aniya et al. 1997). These glaciers have a very large mass balance gradient due to large accumulation and surface ablation (e.g., Lenaerts et al. 2014); additionally, they lose mass from their terminus by frontal ablation consisting of iceberg calving plus melting of the ice front below the water surface. Thus, large mass loss from the glaciers is explained by the negative surface mass balance (SMB) and/or increase in frontal ablation (Minowa et al. 2021). Currently, the largest mass loss in the Patagonian icefields is observed in lake-terminating glaciers, which extend a large ablation area at lower elevations. For those glaciers, the surface ablation dominates the total ablation (Minowa et al. 2021). Bravo et al. (2021a) demonstrated that the rapid mass loss due to negative SMB will continue in the next decades under the series of emission scenarios. Therefore, it is crucial to understand the processes controlling surface ablation and their relation to climate change in Patagonia.

Observations and simulations have suggested that the mean climate in Patagonia is driven by the southern westerly wind (Garreaud et al. 2013; Lenaerts et al. 2014). The westerlies prevail over Patagonia throughout the year and their seasonal and interannual variability control the amount of precipitation and temperature by changing the advection of the air mass (Garreaud et al. 2013), and therefore the SMB (Schaefer et al. 2013, 2015; Lenaerts et al. 2014; Minowa et al. 2017). Several studies have elucidated the characteristics of surface ablation of Patagonian glaciers, which distinguished the contribution of each energy component to the SMB (Takeuchi et al. 1995, 1996; Stuefer et al. 2007; Konya and Matsumoto 2010; Schaefer et al. 2017, 2020; Weidemann et al. 2018b, 2020; Bravo et al. 2021b) (see also Table A1 in the appendix). The sensible heat and shortwave radiation were the most dominant energy fluxes contributing to the glacier melting. However, previous studies were based on fieldwork performed only in summer months (Fukami 1987; Takeuchi et al. 1995, 1996; Konya and Matsumoto 2010; Schaefer et al. 2020), or climate reanalysis datasets (Weidemann et al. 2018b, 2020). Long-term meteorological and SMB observations are still very scarce in the region, and thus the interannual variation in SMB and its controlling processes have not yet been thoroughly investigated.

The climate in Patagonia is influenced by large-scale climate variability. Several studies pointed out that the prevailing westerly wind can be modulated by climate modes dominating the Southern Hemisphere, resulting in variations in temperature and precipitation (Gillett et al. 2006; Garreaud 2009;
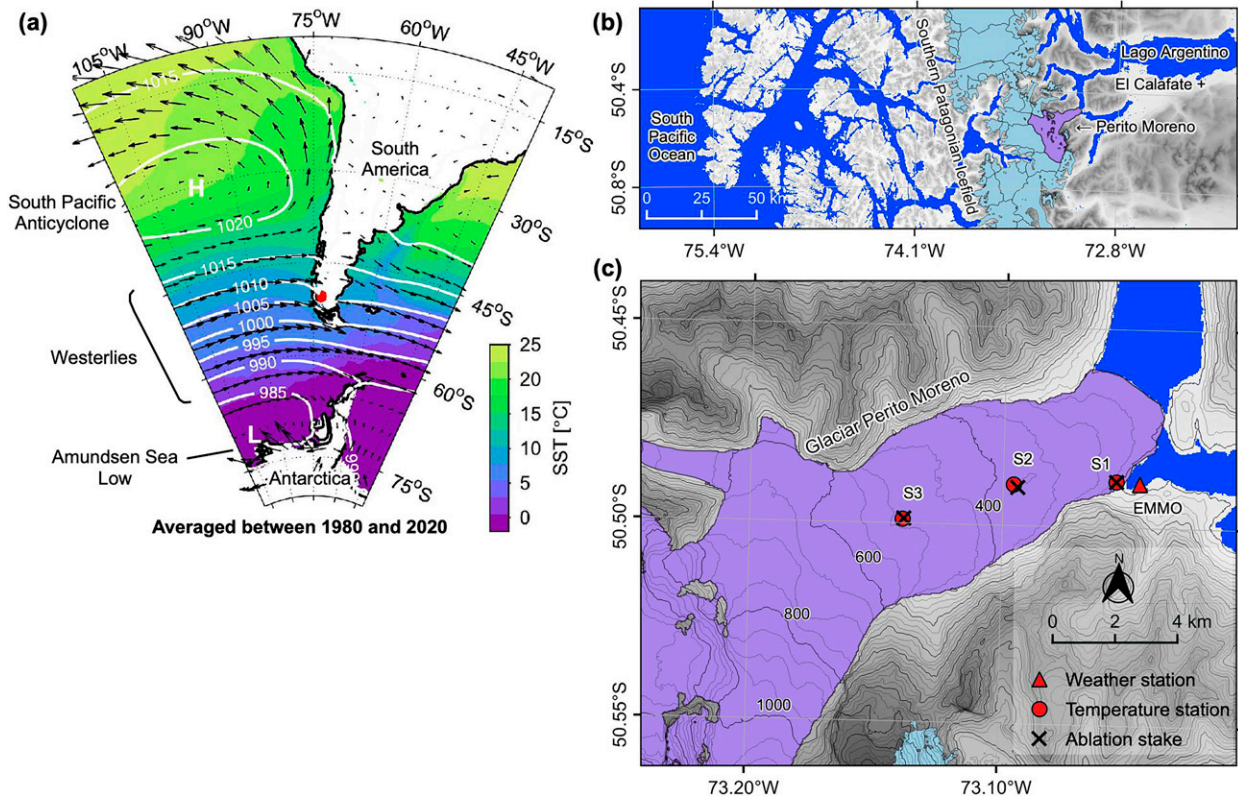

FIG. 1. Maps of the study site: (a) Mean sea level pressure (white contours), wind (black vectors), and sea surface temperature (color coded) of ERA5 reanalysis averaged between 1980 and 2020. The red dot indicates the location of Glaciar Perito Moreno. (b) Topographic map of the study site. Glaciers are indicated in a light-blue area, with Perito Moreno highlighted in purple. (c) Location of the weather station (red triangle), temperature stations (red circles), and ablation stakes (crosses). The background map shows topography with 50-m contour intervals, based on SRTM DEM. Glacier margins are indicated by black lines.

Swart and Fyfe 2012). The Southern Annular Mode (SAM) and El Niño–Southern Oscillation (ENSO) are often used as representative indices in previous studies (Schneider and Gies 2004; Weidemann et al. 2018a; Morales et al. 2020). The SAM is defined by the normalized monthly mean sea level pressure difference between the mid- (40°S) and high latitudes (65°S) (Gong and Wang 1999). It has been suggested that positive SAM can result in warm-air advection to Patagonia by enhancing westerlies, causing an increase in precipitation and temperature, and vice versa (Gillett et al. 2006; Garreaud 2009; Swart and Fyfe 2012). On the other hand, ENSO also plays a role in the climate over Patagonia by modulating the westerlies (Schneider and Gies 2004). Schneider and Gies (2004) analyzed a climate reanalysis dataset to determine possible teleconnections of ENSO with climate in Patagonia. Their study suggested that decreases of the sea level pressure gradient over Patagonia weaken wind speeds during El Niño events, whereas increases of the pressure gradient strengthen wind speeds during La Niña events. However, it is not clear how these climate anomalies modulate the SMB in Patagonia, primarily due to a lack of long-term observations. Since both SAM and ENSO are anticipated to change in the coming decades due to anthropogenic influences (Gillett et al. 2006; Thompson et al. 2011; Jones et al. 2016; Cai et al. 2018; Zambri et al. 2021), understanding the

connection between climate modes and SMB has importance for predicting the future fluctuation of Patagonian glaciers.

In this study, we analyzed meteorological and ablation stake length records between 1996 and 2020 at Glaciar Perito Moreno, located on the east side of the Southern Patagonian Icefield. We investigated hourly to interannual variations in hourly to interannual meteorological records during the period. Energy balance and SMB models were used to calculate a point SMB, which we validated with repeated stake measurements. The dominant process controlling the SMB was investigated by diagnosing the components of energy balance. The 25-yr record of meteorological conditions and SMB were compared with SAM and ENSO.

2. Study site

Glaciar Perito Moreno (50.5°S, 73.2°W) is located in southern Patagonia where the strongest westerlies have been found (Swart and Fyfe 2012; Garreaud et al. 2013) (Fig. 1a). Storm tracks are present year-round at this glacier's latitude, with less seasonality as compared to the Northern Hemisphere (Trenberth 1991; Hoskins and Hodges 2005). Large-scale atmospheric patterns over southern South America were analyzed with climate reanalysis datasets to understand their

influences on the local weather conditions in southern Patagonia (Schneider and Gies 2004; Weidemann et al. 2018a). Development of the South Pacific anticyclone and the Amundsen Sea low causes prevailing westerlies over the southern South America, which are more frequent during the austral summer than austral winter. Overall, this pattern accounts for about 30% of the synoptic weather patterns (Weidemann et al. 2018a). The intensity, location, and course of the westerlies are modulated by the location of the high pressure in the midlatitudes and the low pressure cells in the high latitudes (Fig. 1a), which determines the local weather conditions.

Glaciar Perito Moreno is a lake-terminating glacier flowing from the southern Patagonian icefield, covering an area of 259 km^2 (Fig. 1b) (De Angelis 2014). It flows along the east side of the Andes [2950 m above mean sea level (MSL)] into Lago Argentino (177.5 m MSL) (Fig. 1c). The glacier has shown only small ice-front variations over the last several decades in contrast to other glaciers in Patagonia (Sakakibara and Sugiyama 2014; Minowa et al. 2017). Several factors seem to explain the stable behavior of the glacier, such as the relatively large accumulation-area ratio, shallow bathymetry at the ice front, and steep surface topography around the equilibrium-line altitude (Aniya and Skvarca 1992; Stuefer et al. 2007; Minowa et al. 2015).

Since the approach to the glacier is relatively easy when compared to other Patagonian glaciers, several field observations of SMB were performed in the ablation area of Glaciar Perito Moreno (Takeuchi et al. 1995, 1996; Stuefer et al. 2007). Takeuchi et al. (1995) carried out the first meteorological observations on the glacier over two weeks in November, calculating its energy balance. They found that the net shortwave radiation and sensible heat flux dominate the energy source in surface ablation. Stuefer et al. (2007) measured the ablation with stakes deployed over the ablation area ranging between approximately 200 and 700 m MSL for 7 years following 1995. A high surface ablation reaching 18 m water equivalent (w.e.) yr^{-1} was measured at the lowest stake. The stable glacier behavior and relatively easy access are favorable for long-term monitoring of SMB and meteorological conditions near the glacier front.

3. Methods and data

a. Meteorological records

We recorded local weather at several automatic weather stations (AWSs) located on the bedrock near the glacier front and on the glacier surface (Fig. 1c). Tables A2 and A3 in the appendix respectively summarize the list of weather stations and their observation periods and locations and the list of parameters used in this study. A long-term AWS, named Estación Meteorológica Moreno (EMMO), has been continuously operating since late 1995 (Stuefer 1999; Stuefer et al. 2007), located on the bedrock 450 m southeast of the glacier front (Fig. 1c). EMMO measures air temperature, relative humidity, air pressure, downward shortwave radiation, wind speed, and wind direction at 1-h intervals (Table A3). Except for the air temperature, there are data gaps in 2001 and 2003

due to a datalogger failure. Data gaps for the air temperature were complemented by a backup temperature logger (Ondotori TR52) mounted on the same pole. In February 2016, we installed a weather station (Vaisala WXT520) (EMMO2) on the same pole. While otherwise having the same meteorological parameters as EMMO, it also measures liquid precipitation by means of a sensor sensitive to raindrop intensity. During the field campaigns, several temporal temperature and humidity sensors were also installed on the glacier near the ablation stakes (Table A2). Air temperature and relative humidity, measured on ice every 5 min, were compared with those recorded by EMMO for calibration. The long-term meteorological variables obtained by EMMO were compared with those from EMMO2 between 2016 and 2020 and those from ERA5 between 1996 and 2020 to evaluate aging of the sensors (Table A4 in the appendix), which we discuss in section 5a.

b. Ablation stake measurement

SMB was measured at three stakes located at 230 (S1), 357 (S2), and 485 (S3) m MSL in the ablation area of the glacier (Fig. 1c). S1 has been maintained since 2003 with a 3-yr data gap between 2006 and 2009. We used 5–8 wooden stakes that are 2 m long each, connected by rubber tubes and installed into the ice using a Heucke steam drill (Heucke 1999). To avoid enhancing ice melt, the stakes were painted white. The stake height and the length between the stake top and the ice surface were measured with the help of local mountain guides, who also noted objective weather and glacier surface conditions. In total, we measured the stake length 1017 times, with a mean measurement interval of 4.7 days. At S2 and S3, stakes were installed occasionally during field campaigns on the glacier.

c. Surface mass balance modeling

To investigate energy fluxes contributing to SMB, we solved an energy-balance model at S1 by a glacier energy and surface mass balance model named GLIMB (e.g., Fujita and Ageta 2000; Fujita and Sakai 2014). In this section, we described some essentials of the model. SMB (i.e., b_m; m w.e. day^{-1}) was calculated as

$$b_m = \left(P_s - \frac{H_m}{l_i} + E_v + R_F \right) \bigg/ \rho_w, \tag{1}$$

where P_s is the snowfall rate (mm w.e. day^{-1}), H_m is the heat flux for ice melting (W m^{-2}), l_i is the latent heat of fusion (333.5 kJ kg^{-1} m^{-3}), E_v is evaporation rate (mm w.e. day^{-1}), R_F is the refreeze rate (mm w.e. day^{-1}), and ρ_w is water density (1000 kg m^{-3}).

The heat balance at the glacier surface is described by

$$H_m = R_n + H_s + H_l + H_r + H_g, \tag{2}$$

where R_n is net radiation flux, H_s is sensible heat flux, H_l is latent heat flux, H_r is heat flux from liquid precipitation, and H_g is the conductive heat flux into ice or snow. The flux R_n is calculated as

$$R_n = (1 - \alpha)R_s^{\downarrow} + \varepsilon[R_l^{\downarrow} - \sigma(T_s + 273.2)^4], \tag{3}$$

where α is surface albedo, $R_s^{\downarrow}$ is incoming shortwave radiation (W m^{-2}), ε is the emissivity of the ice/snow surface, σ is the Stefan–Boltzmann constant (5.67×10^{-8} W m^{-2} K^{-4}), and T_s is the surface temperature (°C). The albedo α was determined by the condition of the glacier surface. When bare ice is exposed we assumed it to be 0.3, while we modeled it when the surface is covered by snow based on the relationship between albedo and snow density (Fujita and Ageta 2000). Downward longwave radiation $R_l^{\downarrow}$ is estimated from the dewpoint temperature at the surface with empirical equations that depend on the sunshine ratio (Kondo 1994, 86–91). Relative humidity and saturated vapor pressure were used to calculate the dewpoint temperature. The sunshine ratio was calculated based on the observed downward shortwave radiation and theoretical solar radiation at the top of the atmosphere. The magnitude of possible error in the calculated $R_l^{\downarrow}$ was reported to be 10–20 W m^{-2} (Kondo 1994). The snow or ice surface temperature T_s was determined by an iterative calculation (Fujita and Ageta 2000).

The values of H_s and H_l were calculated with the bulk equations (e.g., Fujita and Ageta 2000; Fujita and Sakai 2014)

$$H_s = c_a \rho_a C U (T - T_s) \quad \text{and} \tag{4}$$

$$H_l = l_e E_v = l_e \rho_a C U [\text{RH} q(T) - q(T_s)], \tag{5}$$

where c_a is the specific heat of air (1006 J kg^{-1} K^{-1}), ρ_a is the density of air (kg m^{-3}), C is the bulk transfer coefficient of sensible and latent heats (0.002), U is the wind speed at a 2-m height (m s^{-1}), T is air temperature (°C), l_e is the latent heat of evaporation of water (2.5×10^6 J kg^{-1}), RH is relative humidity, and q is saturated specific humidity (kg kg^{-1}). The bulk transfer coefficient used in this study was the best-fit value of observations (Kondo and Yamazawa 1986).

The energy received from rainfall was calculated as $H_r = \rho_w c_w P_r (T_r - T_s)$, where c_w is the specific heat capacity of water (4218 J kg^{-1} K^{-1}), P_r is rainfall rate (mm s^{-1}), and T_r is rain temperature, assumed to be equal to air temperature.

The term H_g is calculated from the snow and ice temperature profile with a heat transfer equation (Fujita and Ageta 2000). When the glacier surface is not covered by snow, the temperature profiles were solved from a thermal conduction equation. When the glacier is at melting point or covered by wet snow, H_g is set to zero because of no temperature gradient. When the surface temperature is negative, the heat flux from the glacier to the surface can be calculated (Fujita and Ageta 2000).

ENERGY-BALANCE AND SURFACE MASS BALANCE MODELS

Input data for the model are the daily mean values of downward shortwave radiation, air temperature, relative humidity, and wind speed and the daily amount of precipitation. We used the meteorological record observed hourly between 1996 and 2020 at EMMO. Daily variables, except for precipitation, were calculated from the observed record. Since EMMO is located on bedrock near the terminus of the glacier, air temperature and relative humidity at EMMO could differ from

those on the glacier surface due to the atmosphere–ice interactions (e.g., Petersen and Pellicciotti 2011; Bravo et al. 2019). Thus, we calibrated temperature and relative humidity by comparing them with those observed on the glacier near S1 (Fig. 1c). Linear functions were applied to estimate air temperature (correlation of determination $r^2 = 0.99$; standard deviation SD = 0.3°C) and relative humidity ($r^2 = 0.98$; SD = 2.3%) on the glacier (Fig. A1 in the appendix). The sensitivity of the SMB model for the temperature, relative humidity, and wind speed was evaluated by the one standard deviation of its interannual variation. A continuous liquid precipitation measurement was initiated in 2016. Thus, we used precipitation from the hourly ERA5 total precipitation after calibrating with observations. We find that the observed liquid precipitation is smaller by a factor of 0.37 than the modeled liquid precipitation (Fig. A2 in the appendix), which was used to calibrate the modeled precipitation. Although most of the precipitation falls with liquid precipitation at this altitude of the glacier, solid precipitation can be observed over the winter months. The sensitivity of the SMB, which is dependent on the amount of precipitation, was investigated in section 5c. Last, our hourly meteorological record except for the air temperature has some data gaps, which is 3.2% for the whole observational period. We filled these gaps with the ERA5 hourly reanalysis dataset after calibrating with the observed values (Fig. A3 in the appendix). Linear functions were applied for air temperature, wind speed, downward shortwave radiation, and relative humidity.

d. Reanalysis data and climate proxies

Monthly ERA5 reanalysis data, made available by the European Centre for Medium-Range Weather Forecasts, were used to understand how synoptic-scale climate relates to the SMB. We used the 10-m height wind and mean sea level pressure between 1980 and 2020 over 40°–110°W and 10°–80°S. The product has a horizontal resolution of 0.25° × 0.25° (or approximately 28 × 28 km^2).

We obtained two climate indices, namely SAM and ENSO. We utilized the SAM index calculated by the air pressure observed around 40° and 65°S (Marshall 2003) (https://climatedataguide.ucar.edu/climate-data/). At both latitudes, mean zonal sea level pressure was calculated by six weather stations. For ENSO, we used the bimonthly multivariate ENSO index (MEI.v2; https://psl.noaa.gov/enso/mei/). The index was obtained by the empirical orthogonal function of sea level pressure, sea surface temperature, zonal and meridional components of the surface wind, and outgoing longwave radiation over the tropical Pacific Ocean between 30°S and 30°N and between 100°E and 70°W (Wolter and Timlin 2011).

4. Results

a. Meteorological records

Daily and monthly meteorological records between 1996 and 2020 are shown in Fig. 2. Mean meteorological values at EMMO were 6.7°C for temperature, 67% for relative humidity,
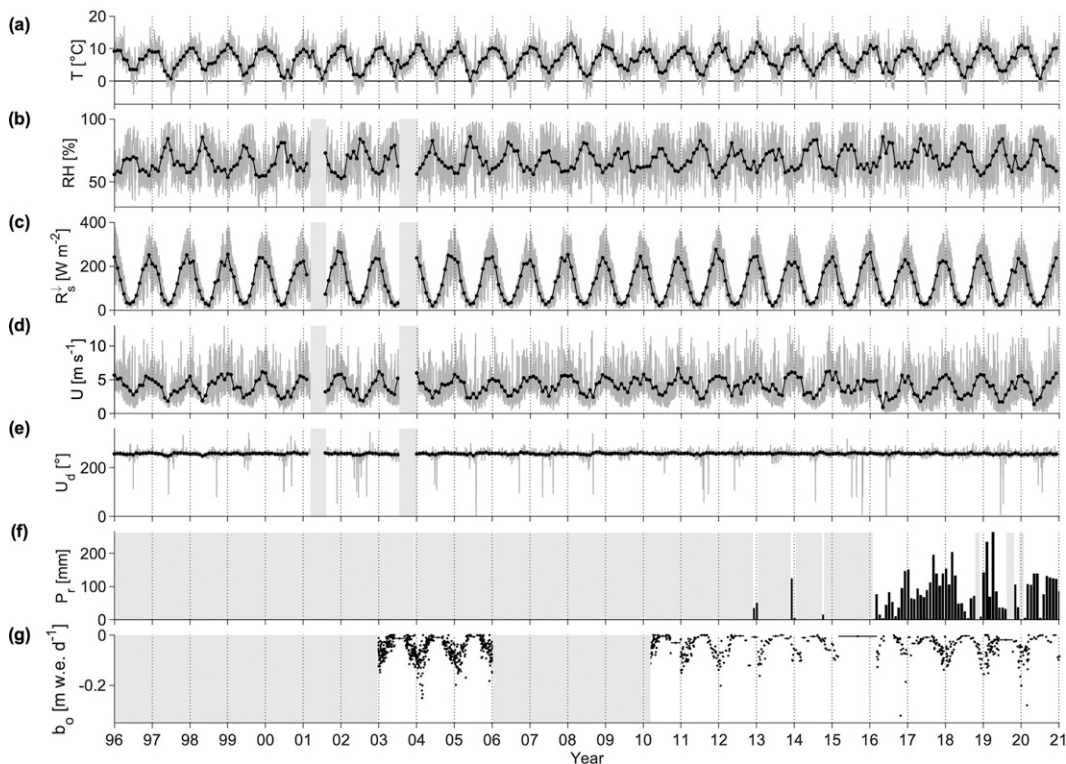
FIG. 2. Meteorological data at EMMO in the vicinity of Glaciar Perito Moreno, measured hourly (gray curves) from 1996 to 2020, along with monthly mean (black dots) (a) air temperature T, (b) relative humidity RH, (c) incoming shortwave radiation $R_s^{\downarrow}$, (d) wind speed U, and (e) wind direction U_d. (f) Monthly total rainfall P_r (black bars). (g) The surface mass balance b_o measured by ablation stakes (black dots). The gray-shaded areas indicate data gaps.

4.1 m s^{-1} for wind speed, and 943 mm for annual precipitation (Table 1). Clear seasonality is visible in air temperature, relative humidity, downward shortwave radiation, and wind speed (Figs. 2 and 3). The monthly mean temperature at EMMO ranged between 0.12° and 11.96°C (Table 1), reaching a minimum in July and a maximum in January (Fig. 3b). During the summer months, we observed stronger wind accompanied by lower humidity than in winter months. Westerly wind dominated the entire period. Occasionally the east wind was observed in winter (Figs. 2e and 3f). Mean monthly wind direction converged between 247° and 264°. Probably because of the limited period of observation for liquid precipitation, seasonality in precipitation was not observed (Fig. 3g).

Mean diurnal variations for each month are shown in Figs. 3h–m. The magnitude varied along the months, but similar diurnal variations were found in temperature, relative humidity, and wind speed (Figs. 3h,i,k). Air temperature, relative humidity, and wind speed covaried during the daytime, which showed 2 h of delay in the daily peaks, compared with downward shortwave radiation and wind direction (Figs. 3h,i,k). As air temperature and wind speed increase in the afternoon, relative humidity decreases. As downward shortwave radiation increased, the wind direction starts to vary about 5° from ~255° to 260° (Figs. 3j,l). Shortwave radiation reaches its daily peak at around 1300–1400 local time (Fig. 3j).

Substantial interannual variabilities in the meteorological records were observed in air temperature and wind speed (Fig. 4). The annual temperature at EMMO showed a warming trend during the study period (Fig. 4a; 0.2° ± 0.1°C decade^{-1}; $p = 0.09$). The warming trend was stronger in the mean seasonal temperature during DJF (Fig. 4d; 0.31° ± 0.1°C decade^{-1}; $p = 0.09$) and SON (Fig. 4c; 0.27° ± 0.2°C decade^{-1}; $p = 0.16$), while there was no clear trend during JJA and MAM (Figs. 4b,e). In the wind speed, there was large year-to-year variability (Fig. 4f). The annual mean wind speed was relatively similar between 1996 and 2006. Subsequently, the positive wind speed anomalies continued for several years between 2007 and 2015, followed by a sudden drop in 2016 and 2017 of 0.79 m s^{-1}. The reduction is due to the wind speed decrease in DJF and MAM (Figs. 2d and 4i,j).

TABLE 1. Summary of mean annual, daily, and monthly ranges of meteorological data obtained between 1996 and 2020.

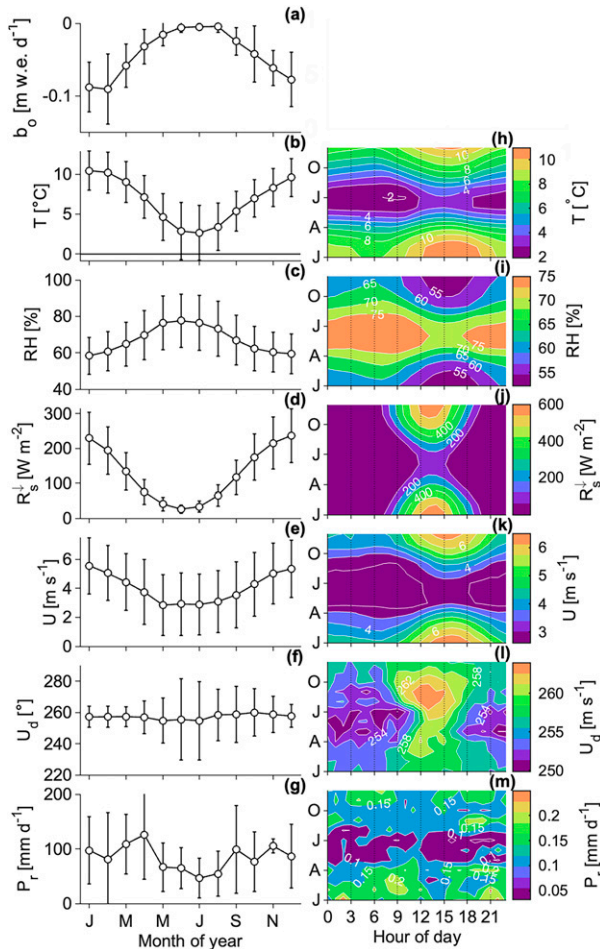|	Units	Mean	Daily range	Monthly range
T	°C	6.71	From −7.01 to 19.29	0.12–11.96
RH	%	67.1	23.9–98.0	52.8–85.9
$R_s^{\downarrow}$	W m^{-2}	128	0–383.8	19.4–267.7
U	m s^{-1}	4.1	0–14.1	0.9–6.6
U_d	°	257	0–346	247–264
P_r	mm	943	0–79.7	3.4–262.4

FIG. 3. Mean monthly (a) surface ablation rate, (b) air temperature, (c) relative humidity, (d) shortwave radiation, (e) wind direction, (f) wind speed, and (g) precipitation. Open circles show the mean value for the meteorological records. Vertical lines indicate 1 standard deviation. Also shown are hourly (h) air temperature, (i) relative humidity, (j) shortwave radiation, (k) wind direction, (l) wind speed, and (m) precipitation for each month (color shading). Mean values are calculated with the hourly record at EMMO between 1996 and 2020, except that the liquid precipitation is based on the data since 2016.

b. Surface mass and energy balances

SMB calculated from individual stake measurements is shown in Fig. 2g. It ranges from 0.02 to -0.32 m w.e. day^{-1} with a mean of -0.06 m w.e. day^{-1}. The monthly SMB showed the minimum in January and February (-0.09 m w.e. day^{-1}) and the maximum in July and August (-0.004 m w.e. day^{-1}) (Fig. 3a). Hence, the glacier melts throughout the year at S1 (Fig. 1c).

The annual mean modeled SMB b_m was -16.3 m w.e. yr^{-1} between 1996 and 2020 (Fig. 5a). The annual mean observed SMB b_o (-16.3 m w.e. yr^{-1}) agreed well with the modeled SMB (-16.5 m w.e. yr^{-1}) for the corresponding years with

the root-mean-square of 0.69 m w.e. yr^{-1}. At this location of the glacier, the SMB was nearly equal to surface ablation. The contribution from snowfall, refreezing and evaporation is negligibly small [Eq. (1)]. The mean difference between SMB and surface ablation was 0.09 m w.e. yr^{-1}. The modeled SMB showed interannual variability ranging from -13.4 m w.e. yr^{-1} in 1997 to -17.8 m w.e. yr^{-1} in 2020 (Fig. 5a). Over the study period between 1996 and 2020, the annual modeled SMB showed a decreased trend with a rate of -0.9 ± 0.3 m w.e. yr^{-1} decade^{-1} ($p = 0.01$). The sensitivity of the SMB model to the input dataset was investigated. It was from -0.95 to 0.96 m w.e. yr^{-1} per $\pm 0.4°C$ for air temperature, from -0.02 to 0.0 m w.e. yr^{-1} per ± 5 W m^{-2} for downward shortwave radiation, from -0.41 to 0.42 m w.e. yr^{-1} per $\pm 2\%$ for relative humidity, and from -0.65 to 0.65 m w.e. yr^{-1} per ± 0.3 m s^{-1} for wind speed. The sensitivity of the SMB for precipitation is described in section 5c.

Interannual variabilities in the energy flux components are indicated in Fig. 5b. Sensible heat flux and net shortwave radiation showed the largest contribution to the point SMB in the ablation zone. The sensible heat flux shows larger interannual variability ranging from 82.6 to 117.2 W m^{-2} than the net shortwave radiation ranging from 80.7 to 94.0 W m^{-2}, and it is similar to the interannual variability of annual SMB (Fig. 5a). The trends in the energy flux components were calculated to be -2.3 ± 0.8 W m^{-2} decade^{-1} ($p < 0.01$) for net shortwave radiation, 3.6 ± 0.3 W m^{-2} decade^{-1} ($p < 0.01$) for net longwave radiation, 2.5 ± 2.4 W m^{-2} decade^{-1} ($p = 0.42$) for sensible heat flux, and 6.1 ± 0.7 W m^{-2} decade^{-1} ($p < 0.01$) for latent heat flux. However, the trends observed in net shortwave radiation and latent heat flux need caution because of the limitation of our AWS. Possible influences on the energy and surface mass balances are discussed in section 5a.

On average, sensible heat flux (mean = 102 ± 26 W m^{-2}; fraction in total energy balance = 58.8%) and net shortwave radiation (86 ± 10 W m^{-2}, 49.9%) showed the greatest contribution to the energy balance (Fig. 6a). The contribution of net longwave radiation was negative (-29 ± 9 W m^{-2}; -16.9%) to the energy balance, indicating a larger longwave going out from the glacier surface than that incoming from the atmosphere. Latent heat flux was 12 ± 15 W m^{-2} (6.8%), indicating a heat supply due to condensation. Heat flux due to liquid precipitation and heat conduction had a minor influence on the energy balance, 1.4 ± 0.6 W m^{-2} (0.8%) and 0.9 ± 1.1 W m^{-2} (0.5%), respectively (Fig. 6a).

Energy flux contributions showed seasonal variability (Fig. 6b). From September to December, the net shortwave radiation flux has a slightly larger contribution to the energy balance than the sensible heat flux. In the rest of the months, the sensible heat flux has the greatest contribution to the energy balance. Longwave radiation showed a negative contribution to the energy balance throughout the year and its seasonal variability was small. Latent heat flux showed a positive contribution between December and May, and a slight negative contribution between August and October. From May to September, the conductive heat flux showed a small positive contribution to the energy balance (Fig. 6c). This means
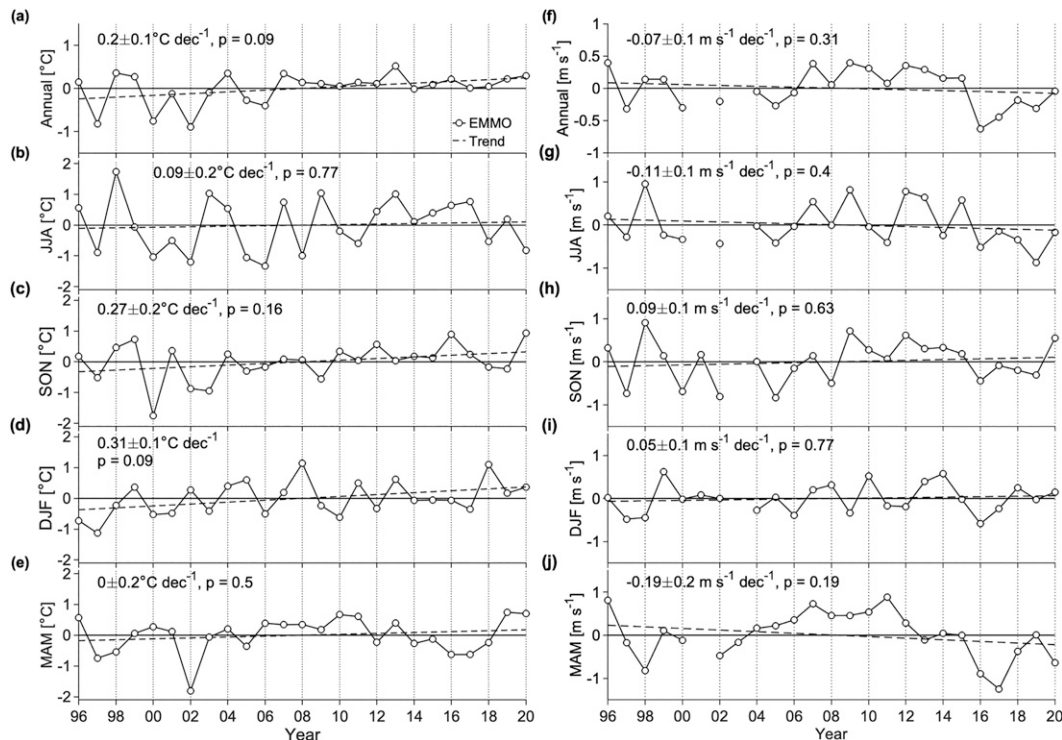
FIG. 4. (a),(f) Annual and (b),(g) JJA; (c),(h) SON; (d),(i) DJF; and (e),(j) MAM seasonal mean (left) air temperature and (right) wind speed anomalies calculated at EMMO between 1996 and 2020. A linear regression is indicated by the black dashed lines. The slope of the regression line and its significance are indicated in each individual panel.

that the heat conducts from the ice body to the glacier surface when the glacier surface is cooled by the atmosphere.

5. Discussion

a. Uncertainties in measurements and calculation

Our meteorological records are long, but they may contain systematic errors due to aging of the sensors and so cause an error in the calculated SMB. To identify possible errors, we analyzed correlation, standard deviation, and trend in the individual daily variables recorded in EMMO and EMMO2 between 2016 and 2020 and in EMMO and ERA5 between 1996 and 2020 (Table A4 in the appendix). Air temperature, relative humidity, and wind speed show a very high coefficient of determination ($r^2 > 0.9$) between EMMO and EMMO2 with limited deviation as compared to the nominal accuracies (Table A3 in the appendix). Air temperature and relative humidity showed a similar trend between 2016 and 2020 in both stations (Table A4), while the trend in wind speed is smaller in EMMO2 (0.57 m s^{-1} decade^{-1}) than in EMMO (1.42 m s^{-1} decade^{-1}). The difference may arise from different sensors: while EMMO uses a conventional anemometer, EMMO2 uses an ultrasonic wind sensor, which is generally more sensitive to a breeze. Although comparing EMMO and ERA5 reanalysis data with the local meteorological dataset is not straightforward due to the large difference in spatial resolution, we find the opposite trend particularly in

relative humidity and shortwave radiation, implying a possibility of a drift in the measured variables (Table A4).

Nevertheless, if we remove the possible systematic errors in shortwave radiation and relative humidity with a best-fit
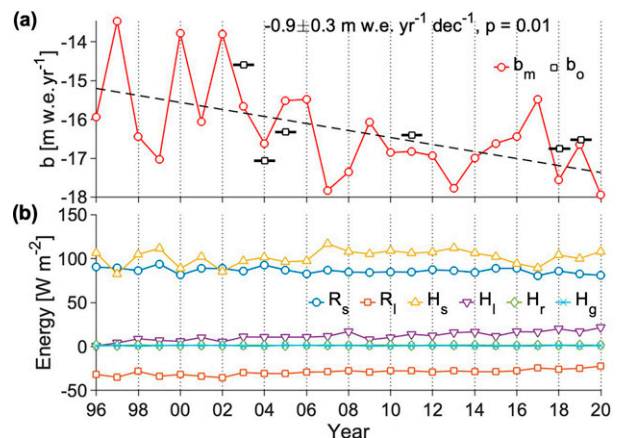

FIG. 5. (a) Annual modeled point surface mass balance at S1 calculated from the stake measurement (b_o; black squares) and SMB model with EMMO station record (b_m; red circles). The best-fit regression line of b_m is indicated in the black dashed line. Also shown are (b) annual energy fluxes for net shortwave radiation R_s, net longwave radiation R_l, sensible heat H_s, latent heat H_l, heat flux from liquid precipitation H_r, and conductive heat flux H_g.
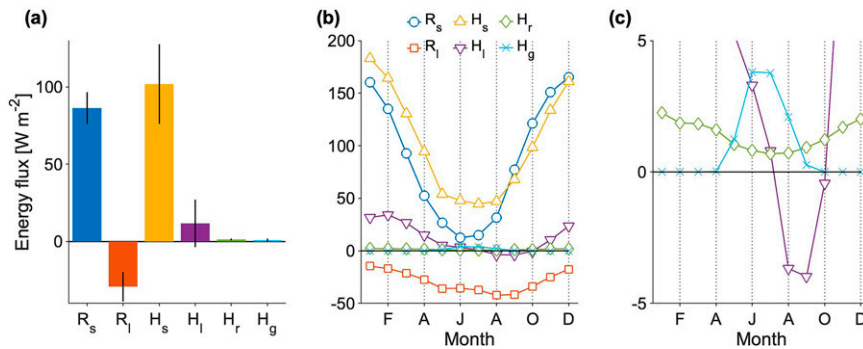
FIG. 6. Mean energy flux components between 1996 and 2020: (a) mean annual energy flux components (colored bars) and 3 standard deviations of annual energy fluxes vertical lines), (b) monthly energy fluxes, and (c) an enlargement of part of (b) to show detail.

linear model, it did not change the mean annual point SMB and mean annual energy balances. The root-mean-square between the observed and modeled SMB was only reduced by 0.03 m w.e. yr^{-1}. Hence, it is unlikely that uncertainties in the measurement influence our calculated mean annual energy and surface mass balances. However, interannual variability, particularly in relative humidity, has higher sensitivity in the SMB model than the other variables (section 4b), because of its impact on the latent heat flux and net longwave radiation. If we exclude the trend observed in relative humidity with a linear model, the calculated trend becomes 1.0 ± 0.5 W m^{-2} decade^{-1} for net longwave radiation and 1.1 ± 0.7 W m^{-2} decade^{-1} for the latent heat flux. This results in a smaller negative trend of SMB, which varied from −0.9 ± 0.3 to −0.4 ± 0.3 m w.e. yr^{-1} decade^{-1}. Therefore, caution is needed in interpreting the influence of net longwave radiation and latent heat flux on the long-term trend in the SMB (Fig. 5).

b. Climate and surface mass balance observed at Glaciar Perito Moreno

The means of meteorological variables show that the glacier is situated in warm, moderately dry, and windy conditions (Table 1; Fig. 2) with respect to other glaciers in the midlatitude locations in Switzerland (Oerlemans et al. 2009), Norway (Giesen et al. 2009), and New Zealand (Cullen and Conway 2015) (Table A1 in the appendix), due to the much lower altitude of the terminus location (Fig. 1), and an influence of rain shadow effect on the lee side of the Andes (Garreaud 2009).

The mean meteorological variables were also compared with previous meteorological observations in Patagonia (Schneider and Gies 2004; Weidemann et al. 2018a; Temme et al. 2020). A first comprehensive meteorological observation in southern Patagonia was performed along with a west-to-east profile across the southern Patagonia around ~52.8°S, approximately 260 km south of Glaciar Perito Moreno (Schneider and Gies 2004; Weidemann et al. 2018a). One of their AWSs, named Puerto Bahamondes, located on the lee side of Gran Campo Nevado Ice Cap, shows similar annual mean air temperature (6.0°C) and seasonal variability [see Table S1 of Weidemann et al. (2018a)]. On the other hand, the meteorological data at

EMMO showed windier and drier conditions and less precipitation than their station (Table 1). We interpret this to be a result of the westerlies flowing over the higher Andean mountains (~3000 m) at Glaciar Perito Moreno than at Gran Campo Nevado Ice Cap (~1500 m), which would cause the air mass to lose more moisture on the windward side, giving place to the drier air mass observed at EMMO. Other west-to-east observations were reported in the southern Patagonian icefield around 51°S, ~50 km south of Glaciar Perito Moreno (Temme et al. 2020). Mean temperature and precipitation were obtained near the terminus of Gray and Tyndall glaciers, which are located on the lee side of the Andes (peaks range from 2000 to 2500 m). Annual mean air temperature and annual precipitation were 6.4°C and 866 mm at Glaciar Gray and 6.0°C and 1212 mm at Glaciar Tyndall, respectively, very similar values to those observed at Glaciar Perito Moreno.

The annual temperature record showed a positive trend of 0.2° ± 0.1°C decade^{-1} over the 25-yr period, which was enhanced in DJF (0.31° ± 0.1°C decade^{-1}) and SON (0.27° ± 0.2°C decade^{-1}) (Figs. 4a,c,d). The observed warming trend in the annual temperature is due to the cold anomaly years in 1997, 2000, and 2002, and almost continuous warm anomaly years since 2007 (Fig. 4a). This trend of annual temperature is larger than the previously reported temperature change. Ibarzabal et al. (1996) found a warming of 0.3°C between 1940 and 1990 (0.06°C decade^{-1}) recorded at a weather station in El Calafate, located ~60 km east of Glaciar Perito Moreno (Fig. 1b). Reanalysis data at the grid point including the glacier (50°S and 75°W) show a warming of 0.5°C between 1960 and 1999 (0.13°C decade^{-1}) (Rasmussen et al. 2007). Weidemann et al. (2018a) reported annual and seasonal mean temperature trends observed by five weather stations across the west-to-east transect at 53°S between 2000 and 2016. A positive trend was found on two out of five weather stations (0.51° and 0.2°C decade^{-1}) (Weidemann et al. 2018a). These results suggest that the warming rate near the icefield has increased in recent decades, particularly in the summer months, which we further discuss with climate indices in section 5d.

Although we observed a warming trend in air temperature and calculated a decrease of SMB over the last 25 years

TABLE 2. The correlation coefficient between surface mass balance and energy fluxes and meteorological parameters. The correlation coefficient was calculated based on annual mean variables averaged between 1996 and 2020. Boldface italic font indicates a correlation significance level at p value 0.05 or better.

	R_s	R_l	H_s	H_l	H_r	H_g	P_r	P_s	T	T_{SON}	T_{DJF}	T_{MAM}	T_{JJA}	U	U_{SON}	U_{DJF}	U_{MAM}	U_{JJA}
r	0.01	***−0.63***	***−0.89***	***−0.65***	***−0.53***	0.32	−0.39	−0.06	***−0.89***	***−0.67***	***−0.56***	***−0.53***	−0.35	***−0.56***	***−0.58***	***−0.46***	−0.19	−0.28
p value	0.96	0.01	0.01	0.01	0.01	0.12	0.06	0.77	0.01	0.01	0.01	0.01	0.09	0.01	0.01	0.02	0.37	0.2

(Figs. 4 and 5), the ice front position and the surface elevation of Glaciar Perito Moreno have been stable (Aniya and Skvarca 1992; Minowa et al. 2015, 2017). This is because the mass balance of a calving glacier is largely influenced by glacier flow, particularly near the terminus (e.g., Meier and Post 1987). Nonetheless, decreased SMB results in surface lowering and an increased amount of meltwater, which can initiate the dynamic retreat of a calving glacier. Because the lower reach of the glacier shows a very high sensitivity to the effective pressure (Sugiyama et al. 2011), that is, ice overburden pressure minus subglacial water pressure, both surface lowering and increases of meltwater would accelerate the ice flow. The balanced mass budget of the glacier would break such as is observed in other calving glaciers in Patagonia (Rivera et al. 2012; Sakakibara et al. 2013; Sakakibara and Sugiyama 2014; Minowa et al. 2021).

c. Processes controlling surface mass balance

The observed and modeled point SMB at S1 show a large negative SMB value, which decreased between −0.4 and −0.9 m w.e. yr^{-1} decade^{-1} over the study period (Fig. 5a). The value is consistent with previous estimates of −18 m w.e. yr^{-1} at the glacier terminus (Stuefer et al. 2007), confirming that a marked negative SMB occurred near the terminus of the glacier in Patagonia compared with other glaciers in the world (e.g., Cuffey and Paterson 2010). The energy flux contributions to SMB indicate the importance of sensible heat flux and net shortwave radiation at the glacier (Fig. 6a), and their contribution varied seasonally (Fig. 6b). Our estimate represents the contribution of mean energy flux better than previous studies, which period of measurement was limited mostly to the summer months, on glaciers located in similar climate settings in Patagonia (e.g., Takeuchi et al. 1995; Schaefer et al. 2020) (see also Table A1 in the appendix). The sensible heat flux also shows a large interannual variability (Fig. 5b), which was first shown by the long-term observational data in this study.

The point SMB and energy flux components were compared with those reported for the other glaciers located at the midlatitudes (i.e., Switzerland, New Zealand, and Norway), which were based on a meteorological dataset covering a whole annual cycle (Oerlemans et al. 2009; Giesen et al. 2009; Cullen and Conway 2015) (Table A1 in the appendix). The point SMB obtained at Glaciar Perito Moreno was several times as large as the other regions because of the high sensible heat flux and net shortwave radiation (Table A1). Compared with other midlatitude glaciers, the glacier terminus is located at a low altitude, resulting in a higher mean temperature. Mean wind speed was higher and relative humidity was lower

than in other glaciers except for Vadret da Morteratsch in Switzerland (Oerlemans et al. 2009). These conditions caused the higher sensible heat flux at Glaciar Perito Moreno [Eq. (4)]. The relatively high temperature also allowed more vapor within the atmosphere [Eq. (5)], causing higher latent heat flux at Glaciar Perito Moreno than the other locations (Table A1). In addition to the warm temperature, much lower precipitation was observed at Glaciar Perito Moreno, where most of the precipitation occurs as rain. This condition causes the ice surface to keep bare ice most of the year except for occasional
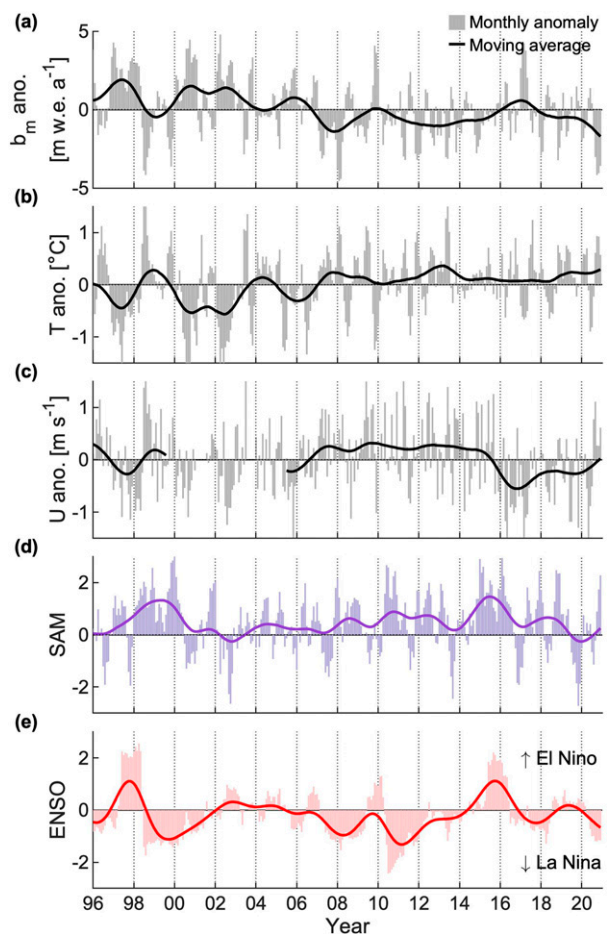

FIG. 7. Modeled monthly point (a) surface mass balance, (b) air temperature at EMMO, and (c) wind speed anomalies and (d) SAM and (e) ENSO climate indices. (a) In (a)–(c), gray and thick black lines respectively indicate monthly values and 3-yr running average. In (d) and (e), thin colored lines indicate monthly indices and thick lines show the 3-yr running average.

TABLE 3. Correlation coefficients between temperature, wind speed, and surface mass balance and ENSO and SAM. In the first row, monthly temperature, wind speed, and surface mass balance were compared with monthly SAM and ENSO. In the other rows, seasonal mean temperature, wind speed, and surface mass balance were compared with seasonally averaged SAM and ENSO. Correlation significance at p values of better than 0.1 and better than 0.05 are indicated by boldface and boldface italic fonts, respectively. Seasonal variability was removed upon comparison from the meteorological and SMB records by subtracting the mean monthly value between 1996 and 2020.

	T–SAM	T–ENSO	WS–SAM	WS–ENSO	b_o–SAM	b_o–ENSO
Monthly						
r	***0.30***	***−0.23***	***0.17***	***−0.22***	***−0.34***	***0.32***
p value	0.01	0.01	0.02	0.01	0.01	0.01
JJA						
r	0.14	−0.09	0.19	−0.02	−0.14	0.15
p value	0.49	0.67	0.35	0.93	0.51	0.48
SON						
r	***0.47***	**−0.37**	***0.42***	−0.27	***−0.53***	**0.39**
p value	0.02	0.06	0.04	0.2	0.01	0.06
DJF						
r	**0.39**	−0.09	0.15	−0.28	**−0.35**	0.31
p value	0.05	0.27	0.48	0.18	0.08	0.14
MAM						
r	0.00	**−0.35**	−0.21	***−0.51***	0.12	**0.40**
p value	0.99	0.09	0.33	0.01	0.56	0.05

snowfall from June to September, which is much longer than the other locations (Oerlemans et al. 2009; Giesen et al. 2009; Cullen and Conway 2015). The lower surface albedo resulted in greater net shortwave radiation at Glaciar Perito Moreno than at other glaciers.

Annual SMB highly correlates with annual mean sensible heat ($r = -0.89$; $p < 0.01$) between 1996 and 2020 (Table 2). The sensible heat flux shows a positive trend of 2.5 ± 2.4 m w.e. yr^{-1} decade^{-1}. These suggest that the calculated interannual variation of SMB was controlled by the variability in sensible heat. For example, a larger interannual variation in the SMB can be found between 1996 and 2005 than in the rest of the years due to low SMB in 1997, 2000, and 2002 (Fig. 5a). For those years, low sensible heat flux was calculated due to low temperature and wind speed (Figs. 4 and 5b). Because the sensible heat flux is controlled by air temperature and wind speed, we further compared the annual mean SMB with annual and seasonal means of temperature and wind speed (Table 2), except for the winter mean due to its limited influence on SMB. Annual temperature shows a strong negative correlation with annual SMB ($r = -0.89$; $p < 0.01$), which was higher than that observed with wind speed ($r = -0.56$; $p < 0.01$) (Table 2). The seasonal mean temperature in SON, DJF, and MAM, and wind speed in SON and DJF also show a negative correlation with annual SMB (Table 2). The highest correlation was found for temperature ($r = -0.68$; $p < 0.01$) and wind speed ($r = -0.58$; $p < 0.01$) in SON among the seasons, implying a large influence on the negative SMB (Fig. 5a). These results suggest that the recent temperature increase is one of the causes of the decrease in SMB, which is modulated by the relatively large interannual variability of the wind speed mainly through the sensible heat flux (Fig. 4).

Latent heat flux and net longwave radiation showed also a positive relationship with the SMB (Table 2). A trend

obtained for latent heat flux (6.1 ± 0.7 W m^{-2} decade^{-1}) and longwave radiation (3.6 ± 0.3 W m^{-2} decade^{-1}) was larger than that obtained for the sensible heat flux. However, we need caution to interpret their influences on the interannual variability in the SMB due to our limitation in the measurement as described in section 5a. Indeed, further evaluation of the measurements as well as replacement of the instruments is necessary to identify the influence in the energy flux component on the long-term trend in the SMB properly. While an accurate conclusion for the influences of latent heat flux and longwave radiation on the trend in the SMB is not conclusive in this study, our data indicate that both latent heat flux and longwave radiation played a role in SMB. Negative correlation was calculated for latent heat flux ($r = -0.51$; $p < 0.01$) and longwave radiation ($r = -0.46$; $p < 0.02$) to the SMB even after removing long-term trends in relative humidity. In addition to this, we find a gradient increase in latent heat flux (1.1 ± 0.7 W m^{-2} decade^{-1}; $p = 0.17$) and longwave radiation (1.0 ± 0.5 W m^{-2} decade^{-1}; $p = 0.04$) over the study period with the detrended relative humidity. The seasonal relative contribution of energy fluxes at S1 shows that from December to March the latent heat flux contributes to melting because the condensation and longwave radiation reduces their negative contribution due to increased radiation from warm, humid air (Fig. 6b). The largest air temperature warming trend over the study period was observed in austral summer (DJF), which can be the result of an increase in latent heat flux and longwave radiation due to the increase of saturated specific humidity in warmer air. On the other hand, a slightly negative value of latent heat flux was obtained between August and October (Fig. 6c). In those months, air temperature is still relatively low (Fig. 3b) and positive conductive heat flux suggested that surface temperature is below zero (Fig. 6c), leading to a limited difference in saturated specific humidity
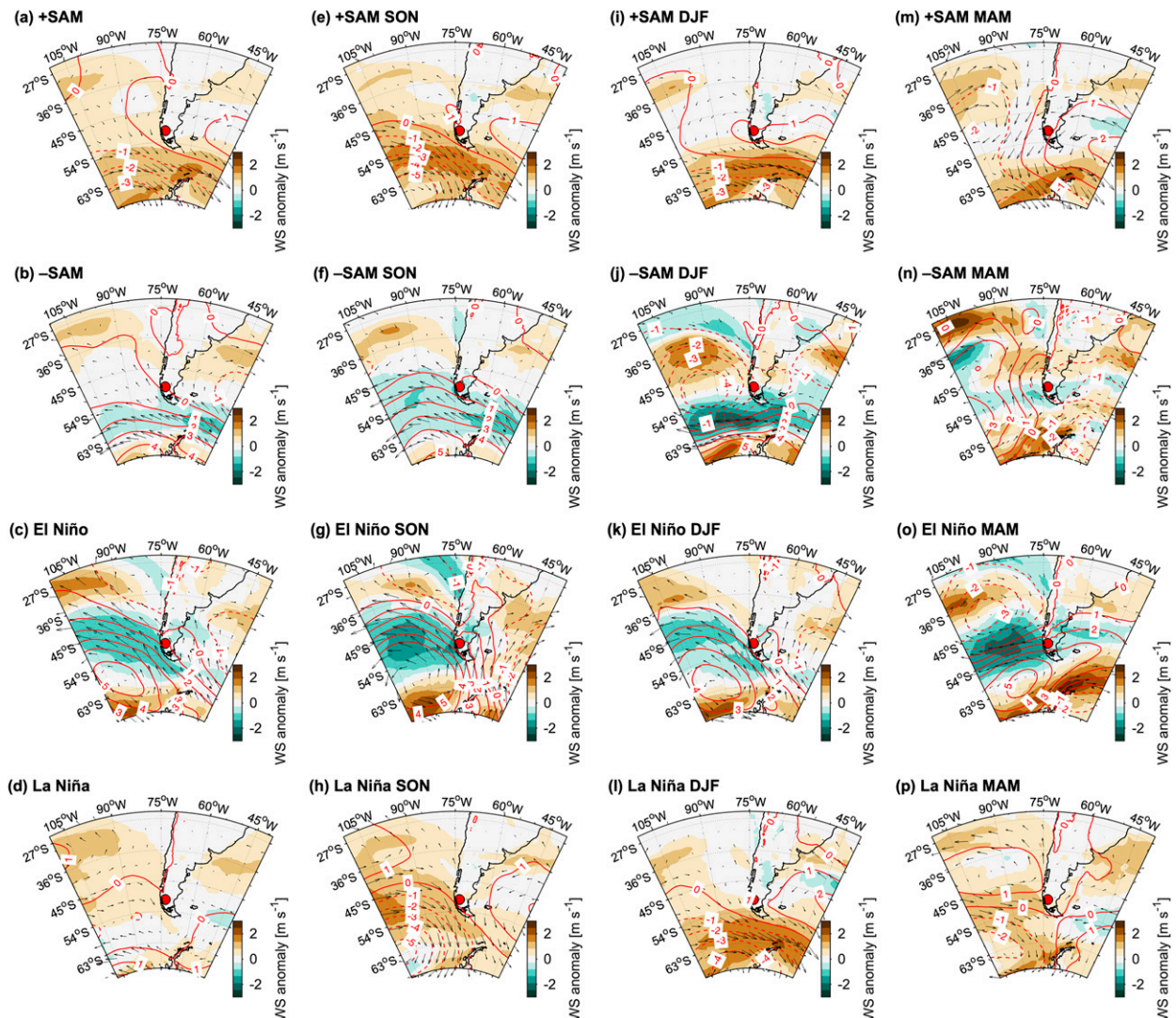
FIG. 8. Mean anomaly of wind speed (black arrows and colored contours) and sea level pressure (red contours) during the climate modes in this region from ERA5 mean monthly between 1996 and 2020 for (a) +SAM, (b) −SAM, (c) El Niño and (d) La Niña. Similar plots are shown for seasonal anomalies in (e)–(h) SON, (i)–(l) DJF, and (m)–(p) MAM. Red circles indicate the location of the glacier.

at the ice–atmosphere boundary [Eq. (5)]. As the relative humidity starts to decrease in August, it causes sublimation or evaporation, suggested by negative latent heat flux (Fig. 5).

Precipitation has a large uncertainty, particularly when it is measured in strong Patagonian westerlies. The numerical climate model also has large uncertainty in precipitation because of the coarse spatial resolution and smoothed topography. It can also change substantially the albedo. Thus, we performed a sensitivity test by changing the precipitation from zero (no precipitation at all) to uncalibrated ERA5 precipitation (2.7 times the input precipitation), to investigate the influence of precipitation on SMB. The mean annual SMB decreased by 0.3 m w.e. yr^{-1} (−1.2%) with no precipitation and increased by 0.1 m w.e. yr^{-1} (0.6%) in the case of uncalibrated ERA5 precipitation from the original mean annual SMB. Net shortwave radiation showed the largest difference

in the sensitivity test among the energy flux components, suggesting the influence on albedo. When there is no precipitation, the albedo remains at 0.3 all the year, while when precipitation occurs as snowfall in winter, it increases the surface albedo and thus decreases the SMB. However, as the temperature is generally above 0°C throughout the year in the lower part of the ablation area (Fig. 3b), the snowfall has a limited effect on SMB. Therefore, the influence of precipitation is limited.

In a temperate glacier, the conductive heat flux can be negligibly small because ice temperature is at the melting point and thus there is no heat conduction (e.g., Cuffey and Paterson 2010). The calculated annual mean conductive heat contributed only 0.5% to the annual melting heat (Fig. 6a). While the calculated conductive heat flux was 0 W m^{-2} between October and April (Fig. 6c), it increased to be as large as 3.8 W m^{-2}
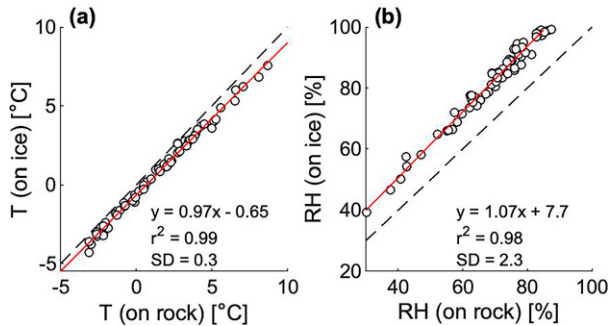
FIG. A1. Scatterplot of (a) daily air temperature and (b) relative humidity between on-ice and on-rock weather stations during July–August 2020. Red lines indicate a linear regression model of the dataset. The black-dashed line indicates a 1:1 correspondence.

from May to September. This is due to heat conduction from the inside of the glacier to its surface when the latter is cooled by low atmospheric temperature. In June, the largest contribution of the conductive heat to the melting heat (2.5%) is calculated. The cooled surface temperature has an impact on the individual energy balance components [Eqs. (3)–(5)] and the heat balance as part of the energy is consumed by increasing surface temperature up to the melting point to start ice melting [Eq. (2)].

The contribution of an individual component of SMB and energy flux can change over the glacier as pointed out by the recent study (Bravo et al. 2021b) while our SMB estimates are spatially limited. Further analysis based on more AWSs and stake records (Fig. 1c) in a follow-up study to estimate glacier-wide SMB and energy balance is needed to better understand the mechanisms controlling the SMB of Patagonian glaciers, although the estimation and validation of spatially distributed meteorological variables is a challenging issue.

d. Relation between large-scale climate anomaly, local meteorological conditions, and surface mass balance

We examined how the global and hemispherical circulation patterns influence the regional meteorological conditions and SMB based on our long-term meteorological and SMB dataset. To do so, we compared the time series of 3-month mean temperature, wind speed, and SMB with SAM and ENSO indices (Fig. 7; Table 3). Upon comparison, seasonal variability was removed from the meteorological and SMB records by subtracting the mean monthly value between 1996 and 2020. The SMB records which removed possible instrumental uncertainties were also compared with SAM and ENSO. It slightly increased the correlation, but no substantial difference was obtained. We also utilized the monthly ERA5 wind speed and mean sea level pressure to understand large-scale atmospheric conditions during positive SAM and La Niña or negative SAM and El Niño (Fig. 8). A seasonal mean anomaly of wind speed and mean sea level pressure was calculated from mean monthly variables between 1996 and
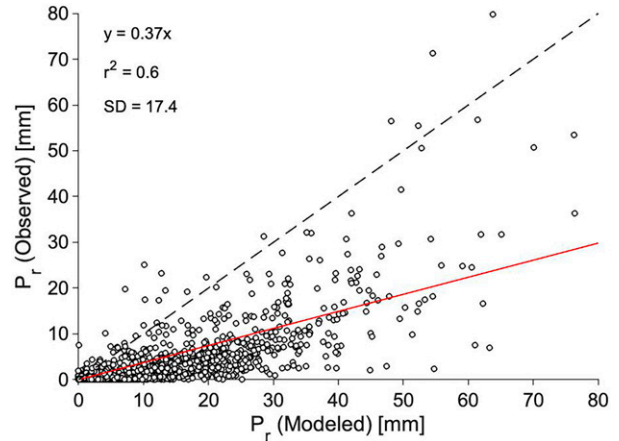

FIG. A2. Scatterplot for modeled and observed daily liquid precipitation utilized on all observational datasets since 2016. Red lines indicate a linear regression model of the dataset. The black dashed line indicates a 1:1 correspondence.

2020 during individual positive SAM and La Niña events or negative SAM and El Niño events.

Our results agree in general with previous studies regarding the relationship between SAM and local meteorological conditions–that positive SAM causes warm-air advection due to the strengthening of westerlies (Gillett et al. 2006; Garreaud 2009; Swart and Fyfe 2012). Weak positive and negative correlations were found between temperature anomalies and SAM ($r = 0.30$; $p < 0.01$) and between SMB anomalies and SAM ($r = -0.34$; $p < 0.01$) on a monthly anomaly basis, respectively (Table 3). The synoptic circulation patterns
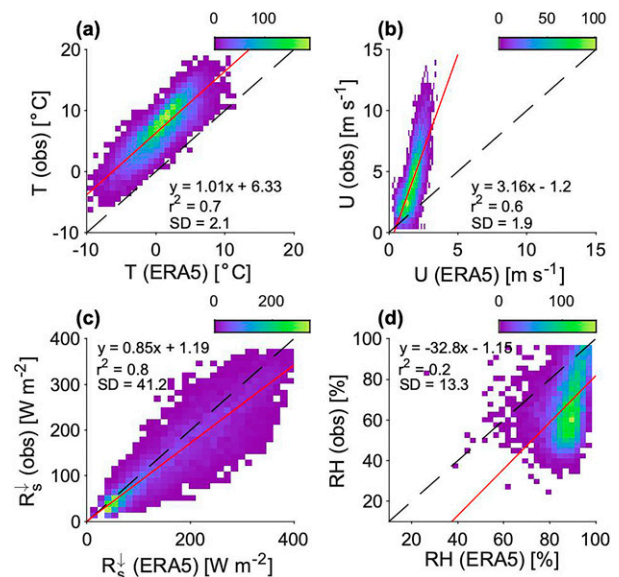

FIG. A3. Density plots of daily mean meteorological parameters observed at EMMO and derived from ERA5 reanalysis dataset between 1996 and 2020. Red lines indicate a linear regression model of the dataset. The black dashed line indicates a 1:1 correspondence.

TABLE A1. Comparison of meteorological conditions, surface mass balance, and energy flux components with previous studies. Location symbols include † for Patagonia, ‡ for New Zealand, * for Switzerland, and ★ for Norway.

Glacier name	Lat (°)	Elev (m MSL)	Period	T (°C)	RH (%)	U (m s⁻¹)	P_r (mm)	b (m w.e. yr⁻¹)	R_s (W m⁻²)	R_l (W m⁻²)	H_s (W m⁻²)	H_l (W m⁻²)	H_r (W m⁻²)	H_g (W m⁻²)	References
Exploradores†	−46.5	200	27 Dec 2006–3 Jan 2007					−22.4	127.3		49.8	26.6	15.0	—	Konya and Matsumoto (2010)
		200	4–7 Jan 2007					−20.1	169.0		18.5	8.1	0.0	—	Konya and Matsumoto (2010)
		191	1 Jan–31 Mar 2015					−23.1	143	−2	65	38	—	—	Schaefer et al. (2020)
Soler†	−46.9	378	1–5 Nov 1985					−10.7	85.5	−24.2	64.1	−8.8	—	—	Fukami (1987)
			25–29 Nov 1985					−21.1	190.6	−24.7	88.2	−3.7	—	—	Fukami (1987)
			15–23 Dec 1983					−30.8	81.0		137.7	82.2	—	—	Kobayashi and Saito (1985)
San Rafael†	−44.7	103	29 Dec 1983–1 Jan 1984					−25.2	110.0	25.5	103.0	40.5	—	—	Ohata (1985)
		1040	19–24 Jan and 29 Jan–1 Feb 1985					−11.4	54.4	–	52.1	28.9	3.5	—	Kondo and Inoue (1988)
Perito Moreno†	−50.4	192	1 Jan 1996–31 Dec 2020	6.71	67.1	4.1	943	−16.3	86	−29	102	12	1.4	0.9	This study
	−50.5	330	12–27 Nov 1993					−26.3	138.9		126.2	−9.3	—	—	Takeuchi et al. (1995)
Tyndall†	−51.2	700	9–17 Dec 1993					−27.4	136.6		111.1	18.5	—	—	Takeuchi et al. (1995)
	−51.13	608	1 Jan–31 Mar 2015					−15.1	94.0	−14.0	65.0	9.0	—	—	Schaefer et al. (2020)
	−51.13	608	1 Jan–31 Mar 2016					−17.1	110.0	−13.0	76.0	9.0	—	—	Schaefer et al. (2020)
Brewstar Glacier‡	−44.08	1760	25 Oct 2010–1 Sep 2012	1.2	78	3.3	~6000[a]	−2.7	48	−27	30	1	2	2	Cullen and Conway (2015)
Morterastch*	46.04	2100	8 Jul 1998–16 May 2007	1.6	64	3.0	~2400[a]	−6.0	73	−38	31	3	—	3	Oerlemans et al. (2009)
Midtdalsbreen★	60.57	1450	7 Sep 2001–6 Sep 2006	−1.2	82	6.6	~3100[a]	−3.8	49	−25	14	4	—	3	Giesen et al. (2009)
Storbreen★	61.60	1570	7 Sep 2001–6 Sep 2006	−1.9	78	3.8	~2600[a]	−2.3	37	−20	15	1	—	3	Giesen et al. (2009)

[a] Note that the precipitation for these glaciers includes solid precipitation.

TABLE A2. List of AWSs, with station names, observation periods, and coordinates. For locations, see Fig. 1c.

Station	Period	Lat (°S)	Lon (°W)	Elev (m MSL)
EMMO	15 Nov 1995–present	50.489	73.049	192
EMMO2	28 Feb 2016–present	50.489	73.049	192
S1	16 Jun–18 Aug 2020	50.489	73.055	230
S2	24 Dec 2012–8 Jan 2013; 7 Dec 2013–2 Jan 2014; 5–20 Oct 2014	50.490	73.096	357
S3	25 Dec 2012–6 Jan 2013; 21 Dec 2013–1 Jan 2014	50.499	73.139	485

show the enhancement of westerlies during positive SAM and reduction during negative SAM (Figs. 8a,b). These correlations and circulation patterns are stronger for SON and DJF (Table 3; see Figs. 8e,f for SON and Figs. 8i,j for DJF).

ENSO showed some magnitude of correlation with temperature, wind speed, and SMB (Fig. 7; Table 3). The monthly temperature anomaly shows a weak negative correlation with ENSO ($r = -0.23$; $p < 0.01$). The circulation pattern indicates a clear reduction in westerlies during El Niño (Fig. 8c). The correlations are especially strong in MAM (Table 3) when a significant reduction in westerlies can be observed during El Niño (Fig. 8o). The correlation coefficient between ENSO and wind speed is -0.51 ($p < 0.01$), and between ENSO and temperature is -0.35 ($p < 0.09$). Thus, ENSO shows positive correlation with SMB ($r = 0.4$; $p < 0.05$) (Table 3). We interpret the reason for the modulation of the westerlies through the atmospheric pressure difference in the region as explained in the early study (Schneider and Gies 2004). During El Niño, the anticyclone in the Pacific Ocean and the low pressure in the Amundsen Sea were weakened (Figs. 8c,g,k,o), while further development of the low pressure in the Amundsen Sea was observed during La Niña (Figs. 8d,h,l,p). These atmospheric conditions resulted in an decrease in air pressure gradient and the westerlies over southern Patagonia during El Niño (Figs. 8c,g,k,o), whereas those increase during La Niña (Figs. 8d,h,l,p).

Overall, our dataset demonstrates that local meteorological conditions and SMB moderately relate to large-scale climate anomalies. One of our limitations is that medium-scale climate influences such as foehns and glacier wind are not considered in this study. It is reported that those local wind features have an impact on the SMB in Patagonia (e.g., Bravo et al. 2019; Temme et al. 2020), which need to be evaluated in future studies. However, the moderate connection still implies that the large-scale climate influences local meteorological conditions

and SMB in the region. Positive SAM trends have been observed over the last several decades with stronger trends in the summer months (Fogt et al. 2009), which would be one of the reasons why we observed a greater warming trend than other studies (e.g., Ibarzabal et al. 1996; Rasmussen et al. 2007) especially in DJF (Fig. 4). Simulation and observation also suggest that the positive SAM results in southward migration of the westerlies (Swart and Fyfe 2012; Perren et al. 2020), yielding warmer and dryer conditions in Patagonia (Garreaud 2018). These changes are anticipated to continue in this century forced by the stratospheric ozone depletion and increased greenhouse gas concentration (Gillett et al. 2006; Arblaster and Meehl 2006). On the other hand, these anthropogenic forcings are expected to lead to a stronger El Niño (Cai et al. 2018). Such conditions occurred in 2016 and showed that interaction between positive SAM and stronger El Niño results in less wind and dry conditions over Patagonia (Garreaud 2018). Substantially negative wind speed anomalies and warm winters but colder summers were recorded at EMMO in 2016 and 2017 (Fig. 4), contributing to the positive SMB anomaly (Fig. 7). This raises a question of whether the anticipated positive trend in SAM and a stronger El Niño accompanied by atmospheric warming but weaker wind conditions result in an increase or decrease in the SMB in Patagonian glaciers in the future. Further observations with a larger number of AWS and mass balance networks, as well as extending our monitoring in the future, are crucial to understand the relationship between large- and medium-scale climate, local meteorological conditions, and the SMB of the rapidly shrinking Patagonian glaciers.

6. Conclusions

One of the longest series of meteorological and ablation stake data in the Patagonian icefields was recorded at Glaciar Perito Moreno between 1996 and 2020 to investigate the climate variability and their influence on glacier SMB. The mean meteorological records indicate that the glacier is

TABLE A3. List of sensor models and nominal accuracy for the individual sensor. Nominal accuracies are indicated in parentheses. An em dash indicates that no sensor is available.

Variable	Units	EMMO	EMMO2	S1–S3
T	°C	HMP35AC (0.1–1.0)	WXT520 (± 0.3)	LR9503 (± 0.15)
RH	%	HMP35AC (1)	WXT520 (± 3)	LR9503 (± 5)
$R_s^{\downarrow}$	W m^{-2}	Pyranometer (10)	—	—
U	m s^{-1}	A100R anemometer (0.13)	WXT520 (± 0.3)	—
U_d	°	W200P wind vane (± 2)	WXT520 (± 3)	—
P_r	mm	—	WXT520 ($<5\%$)	—

TABLE A4. Coefficient of determination r^2 and standard deviation (SD) of daily variables at EMMO, EMMO2, and ERA5. Variables of EMMO were compared with those obtained at EMMO2 between 2016 and 2020 and with those from ERA5 between 1996 and 2020 (in parentheses). The decadal trend of daily variables is also indicated. An em dash indicates that no data are available.

Variable	Units	r^2	SD	2016–20		1996–2020	
				EMMO	EMMO2	EMMO	ERA5
T	°C	0.999 (0.7)	0.14 (2.1)	0.13	0.24	0.18	0.26
RH	%	0.99 (0.2)	1.95 (13.3)	−5.4	−6.1	1.7	−0.7
$R_s^{\downarrow}$	W m^{-2}	— (0.8)	— (41.2)	—	—	−3.1	0.29
U	m s^{-1}	0.97 (0.6)	0.59 (1.9)	1.42	0.57	−0.05	0.02

located in a relatively warm and dry climatic conditions, influenced by strong westerly winds. We observed a warming trend (0.2°C decade^{-1}) resulting in the negative trend in SMB (from −0.4 to −0.9 m w.e. yr^{-1} decade^{-1}). The sensible heat flux showed the largest contribution (59%) to calculated SMB, modulating also its interannual variation due to the interannual variations in air temperature and wind speed. Variations in the latent heat flux and longwave radiation modulated the interannual variation of SMB because of warmer air, although their influence on the long-term trend in the SMB was not clear due to the uncertainty in the relative humidity.

Twenty-five years of meteorological and SMB records were compared with SAM and ENSO. Temperature, wind speed, and SMB showed relationships between SAM and ENSO, especially during SON, DJF, and MAM. Positive SAM and La Niña enhance the westerlies, yielding warmer air temperatures and stronger wind speeds, thus decreasing the SMB. In contrast, negative SAM and El Niño showed opposite influences on air temperature, wind speed, and SMB by reducing the westerlies. These relationships between large-scale climate, local weather and SMB imply that the recent rapid ice mass loss in Patagonia may have been initiated by the large-scale climate variability. Future consideration of the local and mesoscale climate influences, such as foehn and glacier winds, may be beneficial for deepening our understanding of the relationship. Further anthropogenic warming is anticipated in the future, and along with it positive SAM and a stronger ENSO swing. Continuous in situ meteorological and SMB observations are invaluable for understanding the response of Patagonian glaciers to a changing climate.

APPENDIX

Additional Figures and Tables

Figure A1 compares daily air temperature and relative humidity for on-ice and on-rock weather stations. Observed and modeled liquid precipitation are compared in Fig. A2. Figure A3 compares daily mean meteorological parameters observed at EMMO and derived from the ERA5 reanalysis dataset. Table A1 compares meteorological conditions, the surface mass balance, and the energy flux components in this work with those from previous studies. Tables A2 and A3 summarize the list of weather stations, along with their observation periods and locations, and the parameters used in this study, respectively. Table A4 shows comparisons of EMMO variables with those obtained at EMMO2 between 2016 and 2020 and with ERA5 between 1996 and 2020.

REFERENCES

Aniya, M., and P. Skvarca, 1992: Characteristics and variations of Upsala and Moreno glaciers, southern Patagonia. *Bull. Glacier Res.*, **10**, 39–53, https://web.seppyo.org/bgr/pdf/10/BGR10P39. PDF.

——, H. Sato, R. Naruse, P. Skvarca, and G. Casassa, 1997: Recent glacier variations in the Southern Patagonia Icefield, South America. *Arct. Alp. Res.*, **29** (1), 1–12, https://doi.org/ 10.2307/1551831.

Arblaster, J. M., and G. A. Meehl, 2006: Contributions of external forcings to Southern Annular Mode trends. *J. Climate*, **19**, 2896–2905, https://doi.org/10.1175/JCLI3774.1.

Braun, M. H., and Coauthors, 2019: Constraining glacier elevation and mass changes in South America. *Nat. Climate Change*, **9**, 130–136, https://doi.org/10.1038/s41558-018-0375-7.

Bravo, C., D. J. Quincey, A. N. Ross, A. Rivera, B. Brock, E. Miles, and A. Silva, 2019: Air temperature characteristics, distribution, and impact on modeled ablation for the South Patagonia

Icefield. *J. Geophys. Res. Atmos.*, **124**, 907–925, https://doi.org/10.1029/2018JD028857.

——, D. Bozkurt, A. N. Ross, and D. J. Quincey, 2021a: Projected increases in surface melt and ice loss for the Northern and Southern Patagonian Icefields. *Sci. Rep.*, **11**, 16847, https://doi.org/10.1038/s41598-021-95725-w.

——, A. N. Ross, D. J. Quincey, S. Cisternas, and A. Rivera, 2021b: Surface ablation and its drivers along a west–east transect of the Southern Patagonia Icefield. *J. Glaciol.*, **68**, 305–318, https://doi.org/10.1017/jog.2021.92.

Cai, W., and Coauthors, 2018: Increased variability of eastern Pacific El Niño under greenhouse warming. *Nature*, **564**, 201–206, https://doi.org/10.1038/s41586-018-0776-9.

Cuffey, K. M., and W. S. B. Paterson, 2010: *The Physics of Glaciers.* 4th ed. Butterworth-Heineman, 704 pp.

Cullen, N. J., and J. P. Conway, 2015: A 22 month record of surface meteorology and energy balance from the ablation zone of Brewster Glacier, New Zealand. *J. Glaciol.*, **61**, 931–946, https://doi.org/10.3189/2015JoG15J004.

De Angelis, H., 2014: Hypsometry and sensitivity of the mass balance to changes in equilibrium-line altitude: The case of the Southern Patagonia Icefield. *J. Glaciol.*, **60**, 14–28, https://doi.org/10.3189/2014JoG13J127.

Dussaillant, I., and Coauthors, 2019: Two decades of glacier mass loss along the Andes. *Nat. Geosci.*, **12**, 802–808, https://doi.org/10.1038/s41561-019-0432-5.

Fogt, R. L., J. Perlwitz, A. J. Monaghan, D. H. Bromwich, J. M. Jones, and G. J. Marshall, 2009: Historical SAM variability. Part II: Twentieth-century variability and trends from reconstructions, observations, and the IPCC AR4 models. *J. Climate*, **22**, 5346–5365, https://doi.org/10.1175/2009JCLI2786.1.

Fujita, K., and Y. Ageta, 2000: Effect of summer accumulation on glacier mass balance on the Tibetan Plateau revealed by mass-balance model. *J. Glaciol.*, **46**, 244–252, https://doi.org/10.3189/172756500781832945.

——, and A. Sakai, 2014: Modelling runoff from a Himalayan debris-covered glacier. *Hydrol. Earth Syst. Sci.*, **18**, 2679–2694, https://doi.org/10.5194/hess-18-2679-2014.

Fukami, K., 1987: Ablation of ice and heat balance on Soler Glacier, Patagonia. *Bull. Glacier Res.*, **4**, 37–42, https://cetap.cl/wp-content/uploads/2020/03/043.Fukami-Naruse-1987_Ablation-ice-and-heat-balance-Soler-Glacier.pdf.

Garreaud, R., 2009: The Andes climate and weather. *Adv. Geosci.*, **22**, 3–11, https://doi.org/10.5194/adgeo-22-3-2009.

——, 2018: Record-breaking climate anomalies lead to severe drought and environmental disruption in western Patagonia in 2016. *Climate Res.*, **74**, 217–229, https://doi.org/10.3354/cr01505.

——, P. Lopez, M. Minvielle, and M. Rojas, 2013: Large-scale control on the Patagonian climate. *J. Climate*, **26**, 215–230, https://doi.org/10.1175/JCLI-D-12-00001.1.

Giesen, R., L. Andreassen, M. Van den Broeke, and J. Oerlemans, 2009: Comparison of the meteorology and surface energy balance at Storbreen and Midtdalsbreen, two glaciers in southern Norway. *Cryosphere*, **3**, 57–74, https://doi.org/10.5194/tc-3-57-2009.

Gillett, N. P., T. D. Kell, and P. Jones, 2006: Regional climate impacts of the Southern Annular Mode. *Geophys. Res. Lett.*, **33**, L23704, https://doi.org/10.1029/2006GL027721.

Gong, D., and S. Wang, 1999: Definition of Antarctic oscillation index. *Geophys. Res. Lett.*, **26**, 459–462, https://doi.org/10.1029/1999GL900003.

Heucke, E., 1999: A light portable steam-driven ice drill suitable for drilling holes in ice and firn. *Geogr. Ann.*, **81**, 603–609, https://doi.org/10.1111/j.0435-3676.1999.00088.x.

Hoskins, B. J., and K. I. Hodges, 2005: A new perspective on Southern Hemisphere storm tracks. *J. Climate*, **18**, 4108–4129, https://doi.org/10.1175/JCLI3570.1.

Ibarzabal, T. D., J. Hoffmann, and R. Naruse, 1996: Recent climate changes in southern Patagonia. *Bull. Glaciol. Res.*, **14**, 29–36, https://web.seppyo.org/bgr/pdf/14/BGR14P29.PDF.

Jones, J. M., and Coauthors, 2016: Assessing recent trends in high-latitude Southern Hemisphere surface climate. *Nat. Climate Change*, **6**, 917–926, https://doi.org/10.1038/nclimate3103.

Kobayashi, S., and T. Saito, 1985: Heat balance on Soler Glacier. *Glaciological studies in Patagonia Northern Icefield, 1983–1984*, C. Nakajima, Ed., Data Center for Glacier Research, Japanese Society of Snow and Ice, 46–51, https://web.seppyo.org/bgr/pdf/3/BGR3P46.PDF.

Kondo, H., and J. Inoue, 1988: Heat balance on the icefield of San Rafael Glacier, the Northern Patagonia Icefield. *Bull. Glacier Res.*, **6**, 1–8, https://cetap.cl/heat-balance-on-the-icefield-of-san-rafael-glacier-the-northern-patagonia-icefield/.

Kondo, J., 1994: *Meteorology of Water Environment* (in Japanese). Asakura, 348 pp.

——, and H. Yamazawa, 1986: Bulk transfer coefficient over a snow surface. *Bound.-Layer Meteor.*, **34**, 123–135, https://doi.org/10.1007/BF00120912.

Konya, K., and T. Matsumoto, 2010: Influence of weather conditions and spatial variability on glacier surface melt in Chilean Patagonia. *Theor. Appl. Climatol.*, **102**, 139–149, https://doi.org/10.1007/s00704-009-0248-0.

Lenaerts, J. T. M., M. R. van den Broeke, J. M. van Wessem, W. J. van de Berg, E. van Meijgaard, L. H. van Ulft, and M. Schaefer, 2014: Extreme precipitation and climate gradients in Patagonia revealed by high-resolution regional atmospheric climate modeling. *J. Climate*, **27**, 4607–4621, https://doi.org/10.1175/JCLI-D-13-00579.1.

Marshall, G. J., 2003: Trends in the Southern Annular Mode from observations and reanalyses. *J. Climate*, **16**, 4134–4143, https://doi.org/10.1175/1520-0442(2003)016<4134:TITSAM>2.0.CO;2.

Meier, M. F., and A. Post, 1987: Fast tidewater glaciers. *J. Geophys. Res.*, **92**, 9051–9058, https://doi.org/10.1029/JB092iB09p09051.

Minowa, M., S. Sugiyama, D. Sakakibara, and T. Sawagaki, 2015: Contrasting glacier variations of Glaciar Perito Moreno and Glaciar Ameghino, Southern Patagonia Icefield. *Ann. Glaciol.*, **56**, 26–32, https://doi.org/10.3189/2015AoG70A020.

——, ——, ——, and P. Skvarca, 2017: Seasonal variations in ice-front position controlled by frontal ablation at Glaciar Perito Moreno, the Southern Patagonia Icefield. *Front. Earth Sci.*, **5**, 1, https://doi.org/10.3389/feart.2017.00001.

——, M. Schaefer, S. Sugiyama, D. Sakakibara, and P. Skvarca, 2021: Frontal ablation and mass loss of the Patagonian icefields. *Earth Planet. Sci. Lett.*, **561**, 116811, https://doi.org/10.1016/j.epsl.2021.116811.

Morales, M. S., and Coauthors, 2020: Six hundred years of South American tree rings reveal an increase in severe hydroclimatic events since mid-20th century. *Proc. Natl. Acad. Sci. USA*, **117**, 16816–16823, https://doi.org/10.1073/pnas.2002411117.

Oerlemans, J., R. H. Giesen, and M. R. Van den Broeke, 2009: Retreating alpine glaciers: Increased melt rates due to accumulation of dust (Vadret da Morteratsch, Switzerland). *J. Glaciol.*, **55**, 729–736, https://doi.org/10.3189/002214309789470969.

Ohata, T., H. Kondo, and H. Enomoto, 1985: Meteorological observations at San Rafael Glacier. *Glaciological Studies in Patagonia Northern Icefield 1983–1984*, C. Nakajima, Ed., Data Centre for Glacier Research, 22–31.

Perren, B. B., D. A. Hodgson, S. J. Roberts, L. Sime, W. Van Nieuwenhuyze, E. Verleyen, and W. Vyverman, 2020: Southward migration of the Southern Hemisphere westerly winds corresponds with warming climate over centennial timescales. *Commun. Earth Environ.*, **1**, 58, https://doi.org/10.1038/s43247-020-00059-6.

Petersen, L., and F. Pellicciotti, 2011: Spatial and temporal variability of air temperature on a melting glacier: Atmospheric controls, extrapolation methods and their effect on melt modeling, Juncal Norte Glacier, Chile. *J. Geophys. Res.*, **116**, D23109, https://doi.org/10.1029/2011JD015842.

Rasmussen, L. A., H. Conway, and C. F. Raymond, 2007: Influence of upper air conditions on the Patagonia icefields. *Global Planet. Change*, **59**, 203–216, https://doi.org/10.1016/j.gloplacha.2006.11.025.

Rivera, A., M. Koppes, C. Bravo, and J. C. Aravena, 2012: Little Ice Age advance and retreat of Glaciar Jorge Montt, Chilean Patagonia. *Climate Past*, **8**, 403–414, https://doi.org/10.5194/cp-8-403-2012.

Sakakibara, D., and S. Sugiyama, 2014: Ice-front variations and speed changes of calving glaciers in the Southern Patagonia Icefield from 1984 to 2011. *J. Geophys. Res. Earth Surf.*, **119**, 2541–2554, https://doi.org/10.1002/2014JF003148.

——, ——, T. Sawagaki, S. Marinsek, and P. Skvarca, 2013: Rapid retreat, acceleration and thinning of Glaciar Upsala, Southern Patagonia Icefield, initiated in 2008. *Ann. Glaciol.*, **54**, 131–138, https://doi.org/10.3189/2013AoG63A236.

Schaefer, M., H. Machguth, M. Falvey, and G. Casassa, 2013: Modeling past and future surface mass balance of the Northern Patagonia Icefield. *J. Geophys. Res. Earth Surf.*, **118**, 571–588, https://doi.org/10.1002/jgrf.20038.

——, ——, ——, ——, and E. Rignot, 2015: Quantifying mass balance processes on the Southern Patagonia Icefield. *Cryosphere*, **9**, 25–35, https://doi.org/10.5194/tc-9-25-2015.

——, J. L. Rodriguez, M. Scheiter, and G. Casassa, 2017: Climate and surface mass balance of Mocho Glacier, Chilean lake district, 40°S. *J. Glaciol.*, **63**, 218–228, https://doi.org/10.1017/jog.2016.129.

——, D. Fonseca-Gallardo, D. Farías-Barahona, and G. Casassa, 2020: Surface energy fluxes on Chilean glaciers: Measurements and models. *Cryosphere*, **14**, 2545–2565, https://doi.org/10.5194/tc-14-2545-2020.

Schneider, C., and D. Gies, 2004: Effects of El Niño–southern oscillation on southernmost South America precipitation at 53°S revealed from NCEP–NCAR reanalyses and weather station data. *Int. J. Climatol.*, **24**, 1057–1076, https://doi.org/10.1002/joc.1057.

Stuefer, M., 1999: Investigations on mass balance and dynamics of Moreno Glacier based on field measurements and satellite imagery. Ph.D. dissertation, University of Innsbruck, 174 pp.

——, H. Rott, and P. Skvarca, 2007: Glaciar Perito Moreno, Patagonia: Climate sensitivities and glacier characteristics preceding the 2003/04 and 2005/06 damming events. *J. Glaciol.*, **53**, 3–16, https://doi.org/10.3189/172756507781833848.

Sugiyama, S., P. Skvarca, N. Naito, H. Enomoto, S. Tsutaki, K. Tone, S. Marinsek, and M. Aniya, 2011: Ice speed of a calving glacier modulated by small fluctuations in basal water pressure. *Nat. Geosci.*, **4**, 597–600, https://doi.org/10.1038/ngeo1218.

Swart, N. C., and J. C. Fyfe, 2012: Observed and simulated changes in the Southern Hemisphere surface westerly windstress. *Geophys. Res. Lett.*, **39**, L16711, https://doi.org/10.1029/2012GL052810.

Takeuchi, Y., R. Naruse, and K. Satow, 1995: Characteristics of heat balance and ablation on Moreno and Tyndall glaciers, Patagonia, in the summer 1993/94. *Bull. Glacier Res.*, **13**, 45–56, https://web.seppyo.org/bgr/pdf/13/BGR13P45.PDF.

——, ——, and P. Skvarca, 1996: Annual air-temperature measurement and ablation estimate at Moreno Glacier, Patagonia. *Bull. Glacier Res.*, **14**, 23–28, https://web.seppyo.org/bgr/pdf/14/BGR14P23.PDF.

Temme, F., J. V. Turton, T. Mölg, and T. Sauter, 2020: Flow regimes and föhn types characterize the local climate of Southern Patagonia. *Atmosphere*, **11**, 899, https://doi.org/10.3390/atmos11090899.

Thompson, D. W. J., S. Solomon, P. J. Kushner, M. H. England, K. M. Grise, and D. J. Karoly, 2011: Signatures of the Antarctic ozone hole in Southern Hemisphere surface climate change. *Nat. Geosci.*, **4**, 741–749, https://doi.org/10.1038/ngeo1296.

Trenberth, K. E., 1991: Storm tracks in the Southern Hemisphere. *J. Atmos. Sci.*, **48**, 2159–2178, https://doi.org/10.1175/1520-0469(1991)048<2159:STITSH>2.0.CO;2.

Weidemann, S. S., T. Sauter, R. Kilian, D. Steger, N. Butorovic, and C. Schneider, 2018a: A 17-year record of meteorological observations across the Gran Campo Nevado ice cap in southern Patagonia, Chile, related to synoptic weather types and climate modes. *Front. Earth Sci.*, **6**, 53, https://doi.org/10.3389/feart.2018.00053.

——, ——, P. Malz, R. Jaña, J. Arigony-Neto, G. Casassa, and C. Schneider, 2018b: Glacier mass changes of lake-terminating Grey and Tyndall glaciers at the Southern Patagonia Icefield derived from geodetic observations and energy and mass balance modeling. *Front. Earth Sci.*, **6**, 81, https://doi.org/10.3389/feart.2018.00081.

——, J. Arigony-Neto, R. Jaña, G. Netto, I. Gonzalez, G. Casassa, and C. Schneider, 2020: Recent climatic mass balance of the Schiaparelli Glacier at the Monte Sarmiento Massif and reconstruction of Little Ice Age climate by simulating steady-state glacier conditions. *Geosciences*, **10**, 272, https://doi.org/10.3390/geosciences10070272.

Wolter, K., and M. S. Timlin, 2011: El Niño/Southern Oscillation behaviour since 1871 as diagnosed in an extended multivariate ENSO index (MEI.ext). *Int. J. Climatol.*, **31**, 1074–1087, https://doi.org/10.1002/joc.2336.

Zambri, B., S. Solomon, D. W. J. Thompson, and Q. Fu, 2021: Emergence of Southern Hemisphere stratospheric circulation changes in response to ozone recovery. *Nat. Geosci.*, **14**, 638–644, https://doi.org/10.1038/s41561-021-00803-3.

Zemp, M., and Coauthors, 2019: Global glacier mass changes and their contributions to sea-level rise from 1961 to 2016. *Nature*, **568**, 382–386, https://doi.org/10.1038/s41586-019-1071-0.